Electron Cloud Development in the Proton Storage Ring and in the Spallation Neutron Source

M. T. F. Pivi* and M. A. Furman†
Center for Beam Physics
Accelerator and Fusion Research Division
Lawrence Berkeley National Laboratory, MS 71-R0-259
Berkeley, CA 94720
(Dated: **DRAFT:** October 8, 2002)

We have applied our simulation code "POSINST" to evaluate the contribution to the growth rate of the electron-cloud instability in proton storage rings. Recent simulation results for the main features of the electron cloud in the storage ring of the Spallation Neutron Source (SNS) at Oak Ridge, and updated results for the Proton Storage Ring (PSR) at Los Alamos are presented in this paper. A key ingredient in our model is a detailed description of the secondary emitted-electron energy spectrum. A refined model for the secondary emission process including the so called true secondary, rediffused and backscattered electrons has recently been included in the electron-cloud code.

PACS numbers: 29.27.Bd,79.20.Hx,29.20.Dh
Keywords: Electron-cloud effect, secondary electron emission.

I. INTRODUCTION.

The electron cloud effect may limit the performance of intense proton storage rings, causing a fast instability that may be responsible for proton losses and collective beam motion above a certain current threshold, accompanied by a large number of electrons. Electron-cloud dedicated studies have been initiated at the Spallation Neutron Source (SNS) under construction at the Oak Ridge National Laboratory (ORNL). It is becoming progressively clear that the electron-cloud effect plays an important role in the high-intensity instability which has been observed in the PSR at the Los Alamos National Laboratory (LANL) for more than 13 years. This instability is now believed to be due to the collective coupling between an electron cloud and the proton beam [1, 2]. Such instability is a particular manifestation of the electron-cloud effect (ECE) that has been observed or is expected at various other machines. In this article we present simulation results for the SNS and for PSR ring obtained with the ECE code that has been developed at LBNL over the past 6 years. In all results presented here, the proton beam is assumed to be a static distribution of given charge and shape moving on its nominal closed orbit, while the electrons are treated fully dynamically. Furthermore, we can infer details of the electron cloud in the vicinity of the proton beam, such as the neutralization factor, which is important for a self-consistent treatment of the coupled e-p problem [3]. Current instability threshold, growth rate and frequency spectrum are deferred to future studies.

*Electronic address: mpivi@lbl.gov
†Electronic address: mafurman@lbl.gov

TABLE I: Simulation parameters for the PSR and SNS.

Parameter	Symbol	PSR	SNS
Ring parameters			
Proton beam energy	E, GeV	1.735	1.9
Dipole field	B, T	1.2	0.78
Bunch population	N_p, $\times 10^{13}$	5	20.5
Ring circumference	C, m	90	248
Revolution period	T, ns	350	945
Bunch length	τ_b, ns	254	700
Gauss. tr. beam size	σ_x, σ_y, mm	10, 10	···
Flat tr. beam size	r_x, r_y, mm	···	28, 28
Beam pipe semi-axes	a, b, cm	5, 5	10, 10
Simulation parameters			
Proton loss rate	$p_{\rm loss}$, $\times 10^{-6}$	4	1.1
Proton-electron yield	Y,	100	100
No. kicks/bunch	N_k	1001	10001
No. steps during gap	N_g	400	1000
Max sec. yield	$\delta_{\rm max}$	2.0	2.0
Energy at yield max	$E_{\rm max}$, eV	300	250
Yield low energy el.	$\delta(0)$	0.5	0.5
Rediffused component	$P_{1,r}(\infty)$	0.74	0.2

II. PHYSICAL MODEL.

A. Sources of electrons.

The electron production may be classified into: (1) electrons produced at the injection region stripping foil (2) electrons produced by proton losses incident the vacuum chamber at grazing angles (3) secondary electron emission process and (4) electrons produced by residual gas ionization. The two main sources of electrons consid-

ered for proton storage rings at the SNS and the PSR, are lost protons hitting the vacuum chamber walls, and secondary emission from electrons hitting the walls (the electron cloud in the vicinity of the stripper foil is not modelled here). Although our code accommodates other sources of electrons, we have turned them off for the purposes of this article, as they are negligible compared to those above.

B. Secondary emission process

The SEY $\delta(E_0)$ and the corresponding emitted-electron energy spectrum $d\delta/dE$ (E_0 = incident electron energy, E = emitted secondary energy) are represented by a model described in detail elsewhere [4]. The parameters related to the secondary emission process were obtained from detailed fits to the measured SEY of stainless steel [5]. The main SEY parameters are the energy $E_{\max}$ at which $\delta(E_0)$ is maximum, and the peak value itself, $\delta_{\max} = \delta(E_{\max})$ (see Table I). For the results shown below, we do take into account the elastic backscattered and rediffused components of the secondary emitted-electron energy spectrum $d\delta/dE$.

The conventional picture of secondary emission, which we base on various reviews of the subject [6–8], can be summarized as follows: when a steady current I_0 of electrons impinges on a surface, a certain portion I_e is backscattered elastically while the rest penetrates into the material. Some of these electrons scatter from one or more atoms inside the material and are reflected back out. These are the so-called "rediffused" electrons, and we call the corresponding current I_r. The rest of the electrons interact in a more complicated way with the material and yield the so-called "true secondary electrons," whose current we call I_{ts}. The yields for each type of electron are defined by $\delta_e = I_e/I_0$, $\delta_r = I_r/I_0$, and $\delta_{ts} = I_{ts}/I_0$, so that the total SEY is

$$\delta = (I_e + I_r + I_{ts})/I_0 \tag{1a}$$
$$= \delta_e + \delta_r + \delta_{ts} \tag{1b}$$

Experimental data [6, Sec. 3.7], [7, Sec. 4.1.2.2] suggests that a sensible form for $\delta_e(E_0, \theta_0)$ and $\delta_r(E_0, \theta_0)$ at normal incidence ($\theta_0 = 0$) might be given by

$$\delta_e(E_0, 0) = P_{1,e}(\infty) + (\hat{P}_{1,e} - P_{1,e}(\infty))e^{-(|E_0 - \hat{E}_e|/W)^p/p}. \tag{2}$$

$$\delta_r(E_0, 0) = P_{1,r}(\infty)\left[1 - e^{-(E_0/E_r)^r}\right]. \tag{3}$$

while the energy dependence of $\delta_{ts}(E_0, 0)$ is well fit experimentally [6, 8] by an approximately universal [9] function that allows good fit to the experimental data

$$\delta_{ts}(E_0, 0) = \hat{\delta}\frac{s\ (E_0/\hat{E})}{s - 1 + (E_0/\hat{E})^s} \tag{4}$$

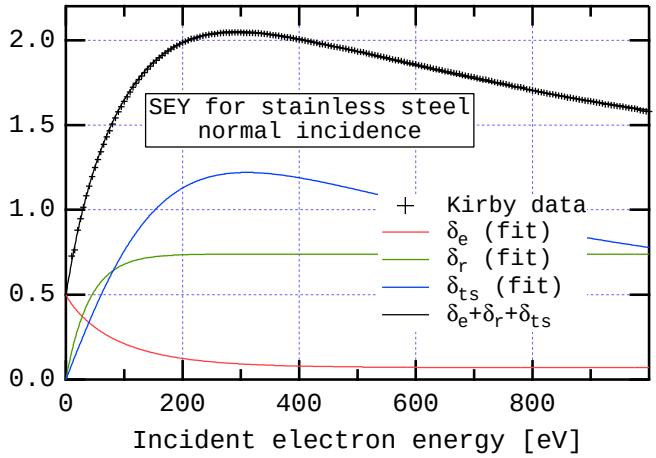

FIG. 1: (Color) The SEY for stainless steel for SLAC standard 304 rolled sheet, chemically etched and passivated but not conditioned. The parameters of the fit are listed in Table II. Data courtesy R. Kirby.

Simulation results are very sensitive to the model for: (1) the energy spectrum of the secondary emitted-electrons [4, Sec. IV], (2) backscattered electron component, in particular to $\delta(0)$. The backscattered component typically becomes more important at low incident electron energies. To account for this behavior we have used a fit extrapolated from data for copper measured at CERN [10]. The value of $\delta(E_0)$ at incident electron energies $E_0 < 10$ eV is an important parameter since it determines the electron survival rate at the end of the gap. This quantity is difficult to measure experimentally, and remains an uncertainty for the model. However, an indication may be given by the decay time of the electron cloud at the end of the beam pulse which has been measured in the PSR [11], see Fig. 2. A long exponential tail seen with 170 ns decay time may imply a high reflectivity for low energy electrons. In Fig. 2, we reproduce the passage of one single PSR beam assuming different values for $\delta(0)$.

C. Simulation Model

The beam-electron interaction and the two-dimensional electric field used in the model are described in detail in [12]. The PSR and the SNS rings store a single proton bunch of length τ_b followed by a gap of length τ_g with a typical current intensity profile shown in Figs. 8 and 10, in line density units nC/m. A Gaussian transverse beam with rms sizes $\sigma_x = \sigma_y = 10$ mm, and the actually measured longitudinal intensity profile are assumed for the PSR. The transverse beam distribution for the SNS is assumed to be constant with $r_x = r_y = 28$ mm. The vacuum chamber is assumed to be a cylindrical perfectly-conducting pipe. The number of electrons generated by lost protons hitting

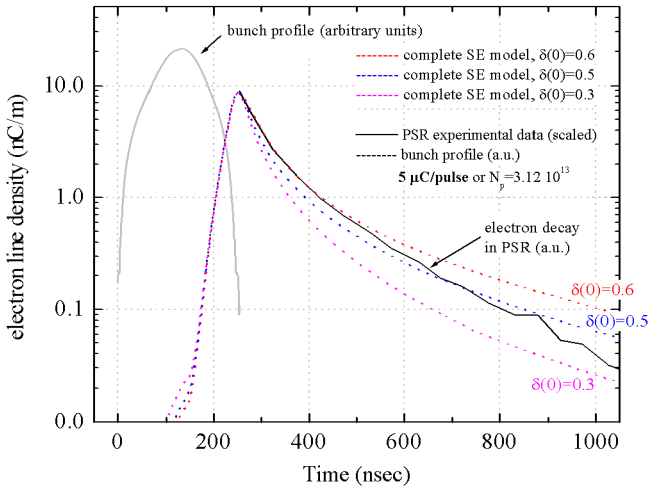

FIG. 2: Experimental data from PSR (courtesy R. Macek) and simulated decay time of the electron cloud at end of a beam pulse with bunch population $N_p = 3.12 \times 10^{13}$ or 5 μC intensity. Different SEY values for low energy electrons, $\delta(0)$, have been assumed in the simulation, with $\delta_{\max} = 2$.

TABLE II: Main parameters of the model, typical values used for the SNS, titanium nitride coated stainless steel.

Backscattered electrons	
$P_{1,e}(\infty)$	0.02
$\hat{P}_{1,e}$	0.5
$\hat{E}_e$ [eV]	0
W [eV]	60
p	1
Rediffused electrons	
$P_{1,r}(\infty)$	0.19
E_r [eV]	0.04
r	0.1
True secondary electrons	
$\hat{E}_{ts}$ [eV]	246
$\hat{\delta}_{ts}$	1.8
s	1.54
Total SEY	
$\hat{E}_t$ [eV]	250
$\hat{\delta}_t$	2

the vacuum chamber wall is $N_p \times Y \times p_{\text{loss}}$ per turn for the whole ring, where Y is the effective electron yield per lost proton, and p_{loss} is the proton loss rate per turn for the whole ring per beam proton. The lost-proton time distribution is proportional to the instantaneous bunch intensity. The electrons are then simulated by macroparticles. The secondary electron mechanism adds to these a variable number of macroparticles, generated according to the SEY model mentioned above. The bunch is divided up into N_k kicks, and the interbunch gap into N_g intermediate steps. The image and space charge forces are computed and applied at each slice in the bunch and each step in the gap. Making the approximation that the electron cloud density is longitudinally uniform, we compute the space-charge forces by means of a two-dimensional electric field. Typical parameter values are shown in Table I. By comparing the measured and simulated decay time of the electron cloud, shown in Fig. 2, we deduce $\delta(0) \simeq 0.5$, and assume this value for the following simulations presented here.

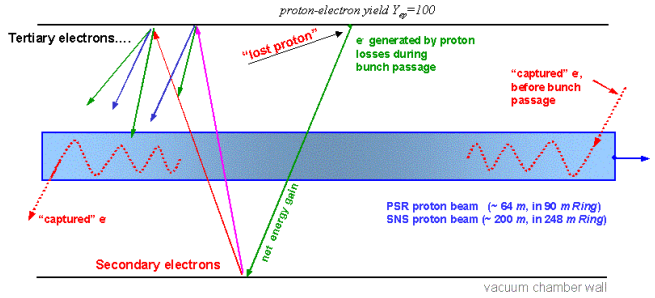

FIG. 3: Electron multiplication mechanism in long proton bunches.

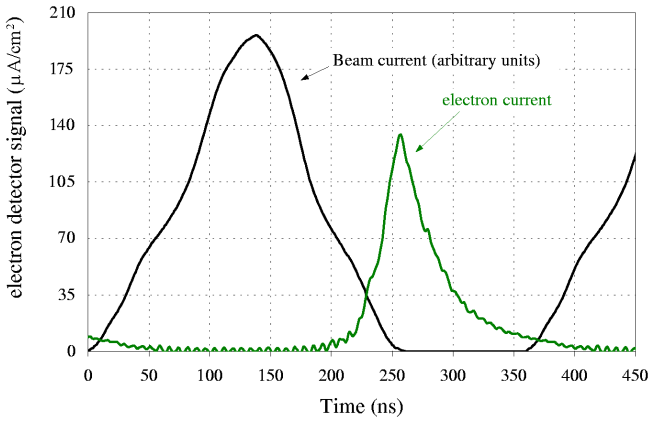

FIG. 4: Measured electron detector (ED02X, located at the injection region) signal at the PSR.

III. RESULTS AND DISCUSSIONS

The possible amplification mechanism which may take place in long-beam storage rings is explained in Fig. 3. An electron present in the vacuum chamber before the bunch passage oscillates in the beam well potential. The oscillation amplitude most likely remains smaller than the chamber radius during the beam passage and the electron is released at the end of the beam passage. On the other hand, electrons generated at the wall by proton losses near the peak of the beam pulse are accelerated and decelerated by the beam potential and hit the oppo-

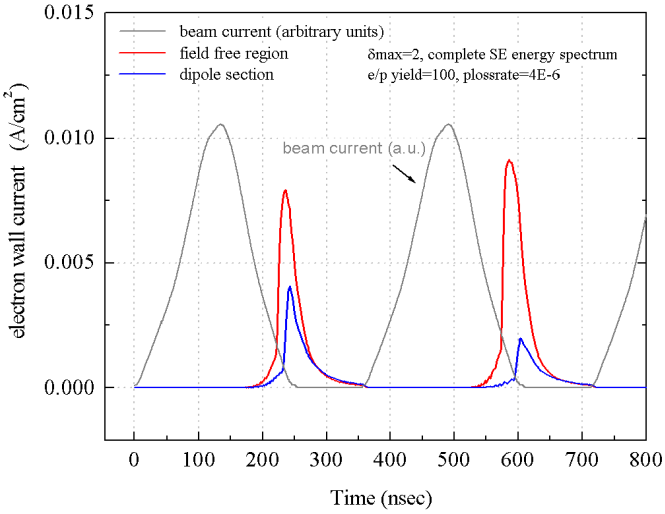

FIG. 5: Simulated current of electrons hitting the surface of the vacuum chamber during the first bunch passages, in a PSR field-free region and a dipole section.

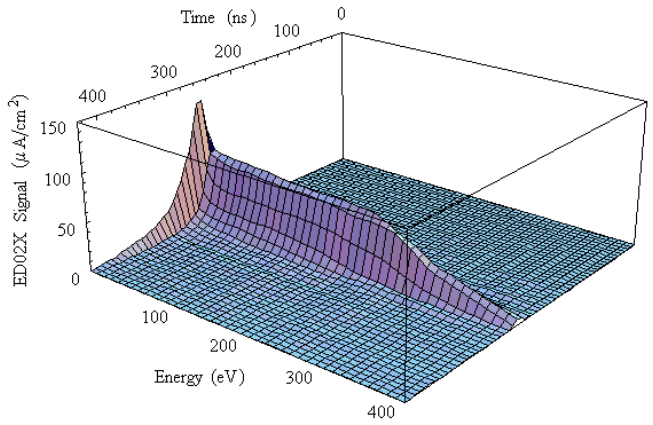

FIG. 6: Measured cumulative energy spectrum of the electrons hitting the wall as a function of time (the origin of time corresponds to the passage of the head of the bunch).

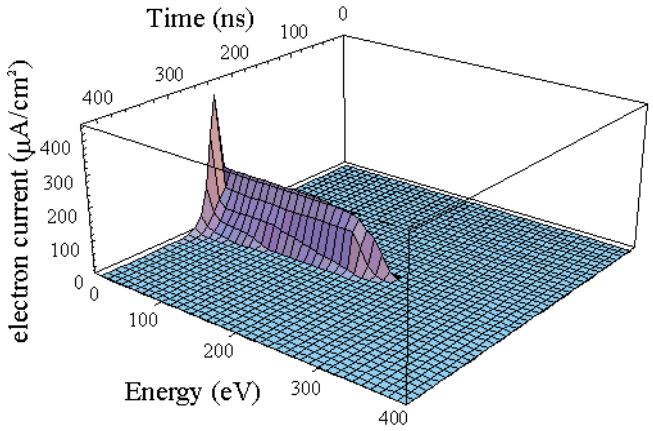

FIG. 7: Simulated cumulative energy spectrum of the electrons hitting the wall as a function of time (the origin of time corresponds to the passage of the head of the bunch).

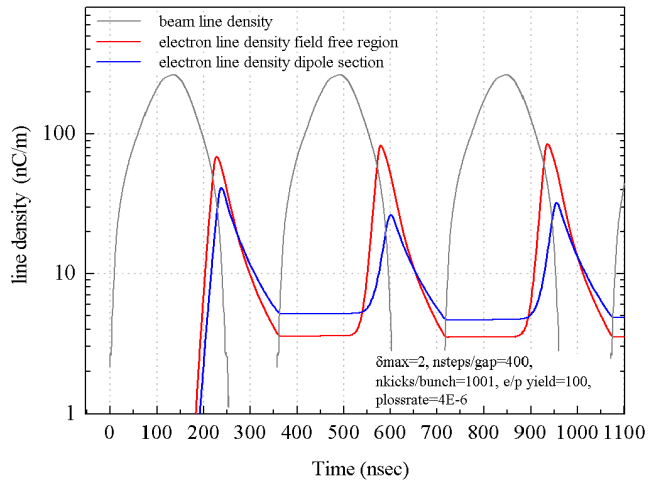

FIG. 8: Simulated electron density during the first bunch passages, in a PSR field-free region and a dipole section. The saturation level is reached after few bunch passages.

site wall with a net energy gain, producing secondary electrons.

Electrons which survive the gap between two bunch passages will increase in number. The electrons gradually increase in number during successive bunch passages until, owing to the space-charge forces, a balance is reached between emitted and absorbed electrons. See also an animation of the PSR electron cloud dynamic during the beam passage at [13].

The current and energy distribution of the electrons hitting the vacuum chamber wall have been measured with dedicated probes [14]. A typical measurement, obtained with the electron detector ED02X at the PSR, is shown in Fig. 4. It should be mentioned that surface conditioning occurred before the measurements were taken. Furthermore, in different sections of the ring, other electron detectors have measured a factor 10 higher electron wall currents. Fig. 5 shows our simulation result, for which we assume unit detector efficiency and acceptance.

By applying a negative potential on the second grid of the electron probe it is possible to select the electrons with an energy sufficient to pass the repeller voltage and thus measure their integrated energy distribution. A typical measurement of the cumulative energy spectrum is shown in Fig. 6; our simulation result is shown in Fig. 7. The measured peak of the electron distribution at the wall (obtained by differentiating the cumulative spectrum with respect to energy) is at ~ 240 eV is in rough agreement with the corresponding simulated number, ~ 180 eV. Furthermore, also in the case of the energy spectrum measurements, detectors located in different sections of the ring have measured higher electron current signals.

The build-up of the electron cloud in a PSR field-free region and a dipole section during the passage of the beam is shown in Fig. 8. The saturation level in the

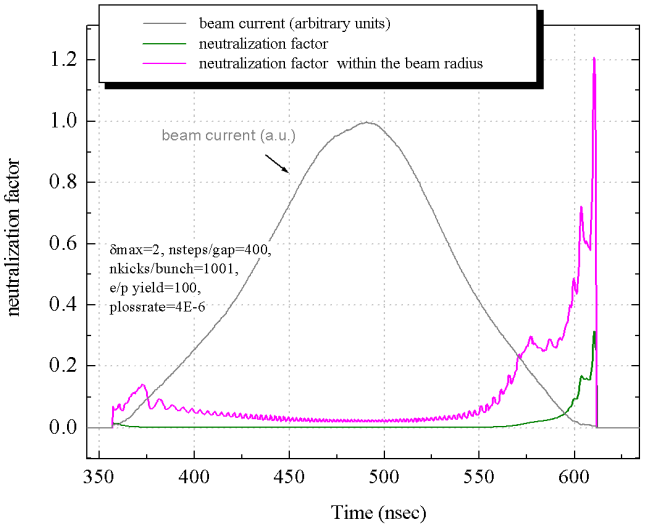

FIG. 9: Simulated electron neutralization factor in a PSR field-free region. The fractional charge neutralization computed within the beam radius region is 2% during the bunch passage, and it exceeds 20% at the tail of the bunch.

PSR is reached after few bunch passages, when assuming $\delta_{\max} = 2$. The estimated peak number of electrons in a field free region is ~ 75 nC/m or 6×10^7 e/cm^3. When assuming $\delta(0) \simeq 0.5$ the simulated electron density in the PSR increases by a factor ~ 3 relative to the $\delta(0) \simeq 0.1$ case (refer to previous results for PSR, see [15]). These are examples of strong parameter sensitivity that calls for further experimental investigations. The neutralization factor or fractional charge neutralization, ratio e/p, during a bunch passage is shown in Fig. 9.

The SNS beam pipe chamber will be coated with TiN. Recent measurements of an as-received sample of the TiN

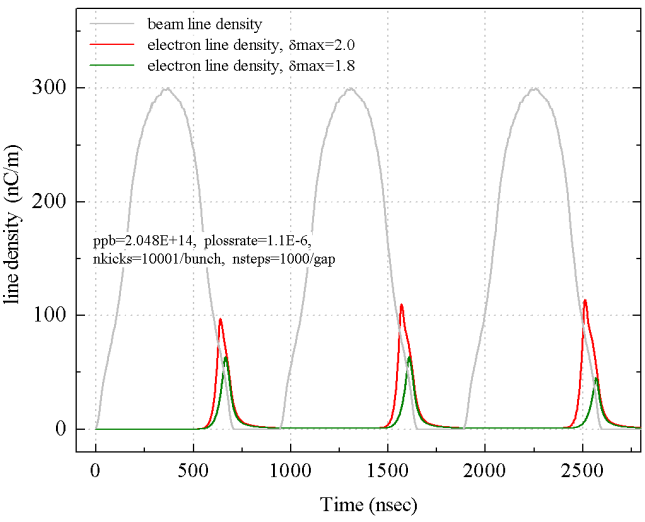

FIG. 10: Simulated electron density during the first bunch passages, in a SNS field-free region, assuming $\delta_{\max} = 2$ and $\delta_{\max} = 1.8$.

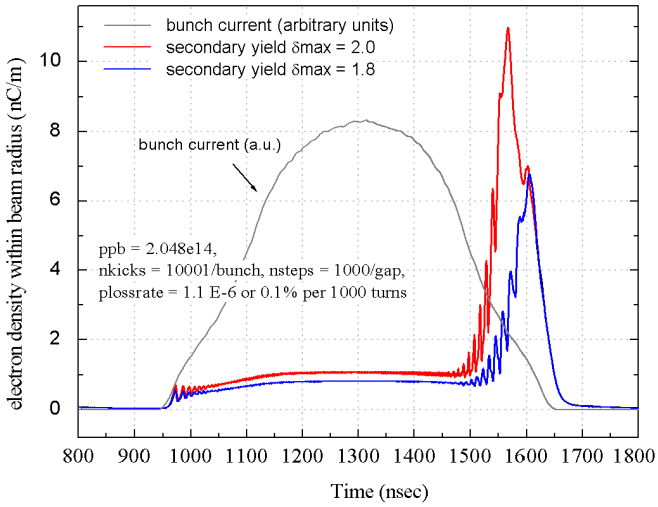

FIG. 11: Simulated electron density computed within the beam radius, in a SNS field-free region, assuming $\delta_{\max} = 2$ and $\delta_{\max} = 1.8$.

coated stainless steel SNS vacuum chamber, has shown a secondary electron yield $\delta_{\max} = 2 \pm 0.2$ [16]. Furthermore, recent secondary yield measurements of TiN coated samples show $\delta_{\max} = 1.9$ [17].

Due to the large electron multiplication, we have used a relatively small number of macroparticles generated per bunch passage, which leads, nevertheless, to reasonably stable results in term of the turn-by-turn electron density. The amplification factor per macroparticle may exceed 10^4 during a single bunch passage when $\delta_{\max} = 2$. Simulation results for the SNS obtained with a different code [18] show a qualitative agreement with our results, although they yield a lower estimated electron density at this SEY value [16].

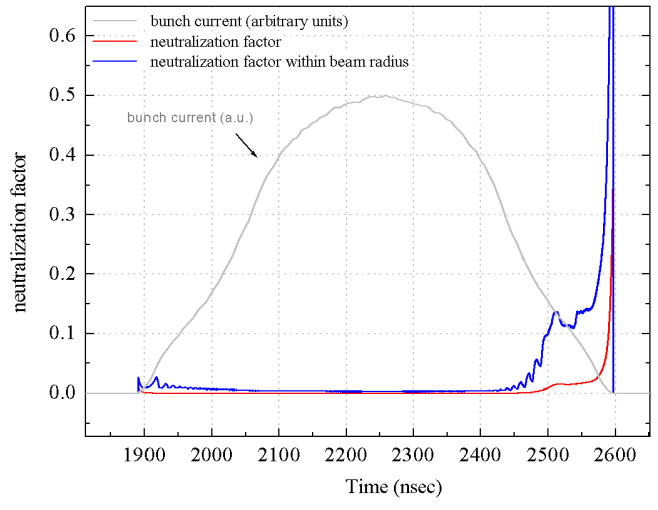

FIG. 12: Simulated electron neutralization factor in a SNS field-free region. The fractional charge neutralization computed within the beam radius region is $\sim 1\%$ during the bunch passage, and it exceeds 10% at the tail of the bunch.

We assume in these simulations that proton losses corresponding to 1.1×10^{-6} protons loss per proton per turn are expected in the SNS ring. For $\delta_{\max} = 2$ and 1.8, the build-up of the electron cloud during the first few bunch passages is shown in Fig. 10 and the electron density computed within the beam radius region is shown in Fig. 11. A total line density of 100 nC/m and a line density within the beam radius region exceeding 10 nC/m are expected in a field-free region. These imply neutralization factors as shown in Fig. 12. In particular the neutralization factor during the bunch passage is 1%, and most of the electrons are contained in the beam radius region.

A 2D particle density histogram of the x-y phase space, averaged over time, is shown in Fig. 13. The electrons are localized most of the time in the inner region of the beam.

The electric field from the cloud leads to a neutralization tune shift which adds to the direct space-charge tune shift. If we make the approximation that the transverse electron-cloud density is uniform within the bunch, a simple estimate can be obtained. Furthermore, the kinetic energy does not exceed few keV, hence the electrons can be considered non-relativistic. Thus the force on any given proton due to the electron cloud is approximately transverse. The tune shift due to electron neutralization may be estimated, for example, for particles in the beam at 25% of the peak intensity where the neutralization factor is $f = 0.13$, by

$$\Delta Q_{ec} = -0.25 f \gamma^2 \Delta Q_{sc} \simeq -0.13 \Delta Q_{sc} = 0.026 \qquad (5)$$

where $\Delta Q_{sc} = -0.2$ is the space charge tune shift and $\gamma = 2.066$ is the usual relativistic factor of the beam.

The possible amplification mechanism which may take place in long-beam storage rings suggest interesting considerations. Electrons generated at the wall by proton losses near the peak of the beam pulse are accelerated and decelerated by the beam potential and hit the opposite wall with a net energy gain, producing secondary electrons. Many generations of secondary electrons may occur during a single bunch passage leading to an high electron cloud density owing to trailing-edge multipacting. In order to verify this assumption, in the simulations, we have artificially truncated the tail of the bunch, while maintaining the same integrated beam charge.

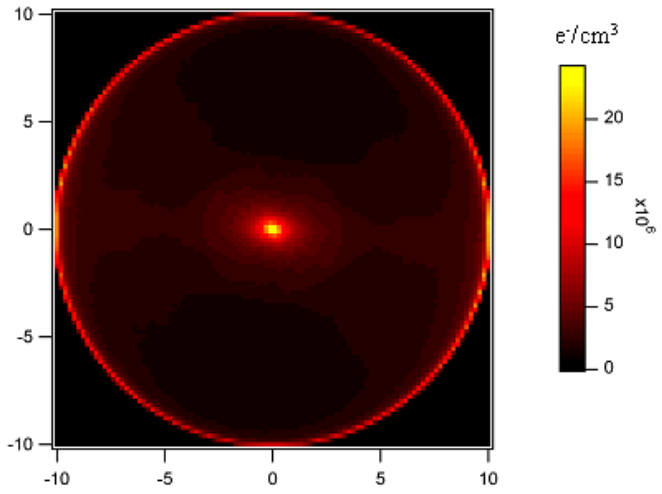

FIG. 13: Image of the time-averaged density of the electron cloud in an SNS field free region.

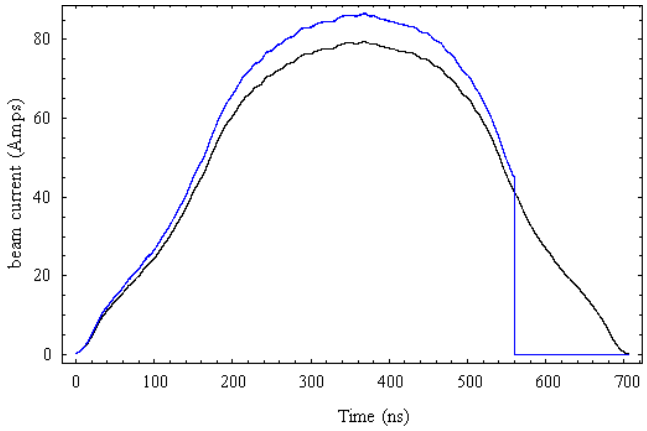

FIG. 14: SNS beam current profile cut at 560 ns, compared to the nominal beam profile.

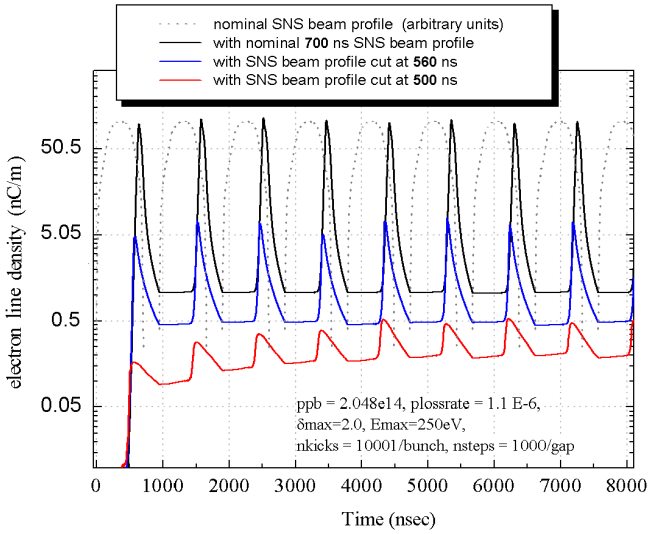

FIG. 15: Simulated electron density in an SNS field-free region, assuming $\delta_{\max} = 2$ and $N_p = 2.05 \times 10^{14}$. We have artificially truncated the tail of the bunch, while maintaining the same integrated beam charge. The density of the electron cloud decrease as the tail of the beam is progressively reduced.

In particular, Fig. 14 shows the modified SNS beam current profile, compared to the nominal beam current profile. The effect of the modification of the beam profile on the formation of the electron cloud is shown in Fig. 15. The density of the electron cloud decreases as the tail of the beam is progressively truncated. A reduction of the beam head profile has the opposite effect of increasing the

electron cloud density. Simulation results for the PSR have shown a similar behavior.

IV. CONCLUSIONS.

We have presented electron cloud simulations for PSR and for the SNS. In the case of the PSR, we have compared our simulation results with measurements of the current and energy distribution of the electrons hitting the vacuum chamber wall. When considering proton losses of 10^{-6} and $\delta_{\max} = 2$, a line density of ≥ 100 nC/m should be expected in an SNS field-free region, with a density exceeding 10 nC/m within the beam radius region. Although the neutralization factor may exceed 10% near the tail of the beam, the resulting electron cloud tune shift is moderate. Linear stability studies and current threshold estimates are deferred to a separate publication [16].

V. ACKNOWLEDGMENTS.

We are particularly indebted to our colleagues of the PSR Instability Studies Program for many stimulating discussions, M. Blaskiewicz, K. Harkay, R. Davidson, H. Qin, P. Channell, T. S. Wang. We are especially grateful to R. Macek for kindly providing us the experimental data and for many valuable discussions. Thanks to R. Kirby, A. Alexandrov, V. Danilov. We are grateful to NERSC for supercomputer support. This work was supported by the US DOE under contract DE-AC03-76SF00098 and by the SNS project (ORNL).

[1] Various contributions in *Proceedings of the ICFA Workshop on Two-Stream Instabilities, Santa Fe, NM, 2000*, http://www.aps.anl.gov/conferences/icfa/two-stream.html. Various contributions to the Two-Stream Instability Workshop, KEK, Tsukuba, 2001 (unpublished) http://conference.kek.jp/two-stream/. Various contributions in *Proceedings of the PAC 2001, Chicago, 2001*, http://pac2001.aps.anl.gov/. Various contributions in the *Proceedings of the ECLOUD-02 workshop, CERN Yellow Report No. CERN-2002-001*, http://slap.cern.ch/collective/ecloud02/, especially the surveys by F. Zimmermann, G. Rumolo, M. Blaskiewicz and R. Macek. Various contributions to the Proceedings of the EPAC02, Paris, 2002 (to be published).

[2] R. Macek, in *Proceedings of the ECLOUD-02 workshop.*

[3] For an updated on the self consistent treatment of the instability see contributions in Physical Review Special Topic, this Special Collection Edition.

[4] M. A. Furman and M. Pivi, LBNL Report No. LBNL-49711/CBP Note 415, 2002, submitted for publication to Physics Review ST.

[5] R. Kirby, private communication.

[6] H. Bruining, *Physics and Applications of Secondary Electron Emission* (Pergamon Press, McGraw-Hill Book Co., New York, 1954).

[7] P. A. Redhead, J. P. Hobson and E. V. Kornelsen, *The Physical Basis of Ultrahigh Vacuum* (Chapman and Hall, London, 1968), Chap. 4 (reprinted by the AIP in 1993 as part of the *American Vacuum Society Classics* series).

[8] H. Seiler, J. Appl. Phys. **54**, 11 (1983).

[9] E. M. Baroody, Phys. Rev. **78**, 780-787 (1950).

[10] V. Baglin, I. Collins, B. Henrist, N. Hilleret and G. Vorlaufer, CERN LHC Project Report No. 472 (unpublished).

[11] M. A. Furman, M. Pivi and R. Macek, LBNL Report (to be published).

[12] M. A. Furman and G. R. Lambertson, LBNL Report No. LBNL-41123/CBP Note 246, SLAC Report No. PEP-II AP Note AP 97.27.

[13] M. Pivi in http://slap.cern.ch/collective/ecloud02/new schedule.html

[14] R. Macek, in *Proceedings of the PAC01, Chicago, 2001*, p. 688.

[15] M. Furman and M. Pivi, in *Proceedings of the PAC01, Chicago, 2001*, p. 708.

[16] M. Blaskiewicz, M. Furman, M. Pivi and R. Macek in Physical Review Special Topic this Special Collection Edition.

[17] T. Toyama, K. Ohmi, in *Proceedings of the ECLOUD-02 workshop.*

[18] M. Blaskiewicz , in *Proceedings of the ECLOUD-02 workshop.*